RSC Advances

ROYAL SOCIETY OF CHEMISTRY

www.rsc.org/advances

Facile synthesis of ordered mesoporous Ni−Zr−Al catalysts with high hydrothermal stability for CO methanation

Qing Liu,[a] Fangna Gu,*[a] Xiaoyan Wang,[a] Guojing Jin,[a]

Huifang Li,[a] Feng Gao,[b] Ziyi Zhong,[b] Guangwen Xu[a] and Fabing Su*[a]

[a] *State Key Laboratory of Multiphase Complex Systems, Institute of Process Engineering, Chinese Academy of Sciences, Beijing 100190, China*

[b] *Institute of Chemical Engineering and Sciences, A*star, 1 Pesek Road, Jurong Island 627833, Singapore*

*Corresponding author. Tel.: +86-10-82544850; Fax: +86-10-82544851. *E-mail address:* fngu@ipe.ac.cn (F. Gu); fbsu@ipe.ac.cn (F. Su).

Abstract

For supported nickel catalysts used for catalytic reactions with presence of water vapor, it is a great challenge to let them have high resistance to sintering, coking as well as water vapor simultaneously. To address this problem, we synthesized a series of ternary ordered mesoporous Ni–Zr–Al metal oxide composites via an evaporation-induced self-assembly (EISA) and applied them for CO methanation reaction. Compared to the ordered mesoporous Ni–Al catalyst, the ordered mesoporous Ni–Zr–Al catalyst showed much improved hydrothermal stability, because the incorporated Zr species could act as the supporter for the OMA framework, effectively preventing it from sintering-caused structural collapse and phase transition during the hydrothermal treatment; Also, in a 120h-lifetime test, the ordered mesoporous Ni–Zr–Al catalyst showed high anti-coking and anti-sintering properties, mainly because of the confinement effect of the mesopore channels as well as the incorporation of the zirconia promoter.

1. Introduction

In recent years, gasification of coal or biomass to syngas and further conversion of the syngas into synthetic natural gas (SNG) via the methanation reaction ($CO + 3H_2 \rightarrow CH_4 + H_2O$, $\Delta H_{298K} = -206.1$ kJ mol^{-1}) has attracted much attention.[1, 2] Due to the exothermic nature of this reaction, the often used supported Ni catalysts suffer from Ni sintering and coke formation during the methanation process.[3, 4] Furthermore, the above sintering processes can be accelerated by the presence of water vapor,[5] which is one of the products of methanation reaction. Therefore, it is very important to develop catalysts with high resistance to sintering, coking and water vapor simultaneously.

The most straightforward way of stabilizing metal nanoparticles is to encapsulate them into thermally stable and chemically inert oxide forming core-shell, core-sheath or ordered mesopores-like structrures.[6, 7] By comprehensively considering the scalability, operability and economic cost in synthesis of the above mentioned structures, it seems that the ordered mesoporous material is most feasible for industrial production. The ordered mesoporous supports can not only confine metal nanoparticles in a fixed space to prevent them from sintering and coke formation, but also offer a high surface area for the high dispersion of active metals, thus promising to improve both the activity and long-term stability of the catalysts.[3]

Since the successful synthesis of the ordered mesoporous alumina (OMA) via the one-pot evaporation-induced self-assembly (EISA) strategy by Yuan et al.,[8] the Ni-based OMA materials have been extensively investigated as the heterogeneous catalysts. Although the Ni-based OMA catalysts exhibit high thermal stability at high temperature (900 ^{o}C),[9] their hydrothermal stability is still poor,[10] which seriously inhibits the application of OMA. It is well known that ZrO_2 is an inorganic oxide having both acidic and basic properties, high thermal stability as well as chemical

inertness, and having been reported as the efficient promoter or support in the catalysts for methanation reaction. In these catalysts, the ZrO_2-additive modified the metal-support interaction,[11] improves the metal dispersion[12, 13] and enhances the catalytic performance.[11-14] In addition, as found by Wang et al., the addition of proper amount of ZrO_2 additives can efficiently improve the hydrothermal stability of OMA during boiling water treatment.[10] Hence, it is expected that the addition of ZrO_2 to the Ni-based OMA may play similar function to enhance the hydrothermal stability as well as the catalytic performance of the catalysts.

In this work, we successfully synthesized a series of ordered mesoporous Ni–Zr–Al metal oxide composites via the EISA route, and investigated their hydrothermal stability and catalytic stability. The results show that the ordered mesoporous Ni–Zr–Al catalyst exhibits high hydrothermal stability as well as high anti-coking and anti-sintering properties, due to the confinement effect of the mesopore channels as well as the incorporation of the ZrO_2 species.

2. Experimental

2.1. Catalyst preparation

The chemicals with analytical grade including nickel (II) nitrate hexahydrate ($Ni(NO_3)_2 \cdot 6H_2O$), aluminum isopropoxide ($Al(OPr^i)_3$), 67 wt% nitric acid (HNO_3) and ethanol were purchased from Sinopharm Chemical Reagent Co. Ltd., China, and used without further purification. $(EO)_{20}(PO)_{70}(EO)_{20}$ triblock copolymer (Pluronic P123, typical M_n = 5800) and zirconium *n*-butoxide ($Zr(OBu)_4$) were purchased from Sigma-Aldrich. The commercial porous γ-Al_2O_3 (Zibo Honghe Chemical Co. Ltd., China) with a surface area of 164 $m^2\ g^{-1}$ was calcined at 400 ^oC in air (0.1 MPa) for 2 h prior to use.

The ordered mesoporous Ni–Zr–Al catalysts were prepared by EISA method.[3] In a typical

synthesis, 2.1 g P123 was dissolved in 40.0 mL of anhydrous ethanol, followed with addition of 3.2 mL 67 wt % nitric acid, 4.08 g $Al(OPr^i)_3$ and stoichiometric amounts of $Ni(NO_3)_2 \cdot 6H_2O$ and $Zr(OBu)_4$ in sequence under vigorous stirring. The obtained mixture was covered with PE film and stirred at room temperature for at least 5 h, and was then placed in an oven at 60 °C for evaporation of ethanol for 48 h. The final gel was calcined at 550 °C for 4 h in air (0.1 MPa) at a heating rate of 1 $^oC\ min^{-1}$. The NiO content was fixed at 10 wt% in all catalysts in this work, and the obtained samples were denoted as 10NxZOMA (x = 0, 2, 5 and 10), where x represents the mass percent of ZrO_2.

The preparation of 40ZOMA sample followed procedures similar to that for the preparation of the 10NxZOMA catalysts but without addition of $Ni(NO_3)_2 \cdot 6H_2O$. The 10N40ZOMA catalyst was prepared by an incipient wetness impregnation method. The stoichiometric amount of $Ni(NO_3)_2 \cdot 6H_2O$ was dissolved in a certain amount of ethanol, then the solution was added dropwise to the 40ZOMA powder and dried at room temperature for at least 48 h, followed with calcination at 550 ^oC for 4 h in air (0.1 MPa) at a heating rate of 2 $^oC\ min^{-1}$. In addition, the calcined 10N40ZOMA was reduced at 700 ^oC for 1 h in H_2 flow, and the sample was denoted as 10N40ZOMA-Re. The disordered mesoporous ZrO_2–Al_2O_3 sample was prepared by the wet impregnation method. The stoichiometric quantity of $Zr(OBu)_4$ was dissolved in ethanol, followed with addition of the γ-Al_2O_3 support to form a slurry. The slurry was vigorous stirred at room temperature overnight, and then heated to 70 ^oC to evaporate the liquid, followed with drying at 100 ^oC for 24 h and further calcination at 550 ^oC for 2 h in air (0.1 MPa) with the heating rate of 2 $^oC\ min^{-1}$. The collected sample with a ZrO_2 content of 40 wt% was denoted as 40ZA.

2.2. Catalysts characterization

N_2 adsorption was measured at −196 °C using a Quantachrome surface area & pore size analyzer NOVA 3200e. Prior to the measurement, the sample was degassed at 200 ºC for 4 h under vacuum. The specific surface area was determined according to the Brunauer-Emmett-Teller (BET) method. The pore size distribution (PSD) was calculated based on the Barett-Joyner-Halenda (BJH) method using the adsorption isotherm branch. X-ray diffraction (XRD) patterns in the range of 10.0 to 90.0°(wide angle range) or 0.5 to 5.0° (small angle range) were recorded on a PANalytical X'Pert PRO MPD with a step of 0.02° using Cu Kα radiation (λ=1.5418 Å) at 40 kV and 40 mA. The crystal size of the sample was estimated using the Debye-Scherrer equation. H_2 temperature-programmed reduction (H_2-TPR) and H_2 temperature-programmed desorption (H_2-TPD) experiments were carried out on Quantachrome Automated chemisorption analyzer (chemBET pulsar TPR/TPD) following the procedures reported previously.[15-17] For H_2-TPR, 0.1 g sample was loaded in a quartz U-tube and heated from room temperature to 200 °C at 10 °C min^{-1} and maintained for 1 h under He flow. Then, the sample was cooled to room temperature, followed by heating to 1000 °C with a heating rate of 10 °C min^{-1} in 10 vol% H_2/Ar flow (30 mL min^{-1}). For H_2-TPD, 0.2 g catalyst was used and reduced in situ in a H_2/Ar flow at 700 °C for 1 h. Subsequently, the sample was cooled down to room temperature and saturated with H_2. After removing the physically adsorbed H_2 by flushing with Ar for 2 h, the sample was heated to 600 °C at 10 °C min^{-1} in an Ar flow (30 mL min^{-1}). The consumed or desorbed H_2 was detected continuously as a function of temperature using a thermal conductivity detector (TCD). The dispersion of Ni was calculated using the volume of chemisorbed H_2 based on the formula described in our previous work.[3] The microscopic feature of the samples was observed by field emission scanning electron microscope (SEM) (JSM-6700F, JEOL, Japan) and transmission electron microscopy (TEM) (JEM-2010F, JEOL, Japan). The elemental mapping was also performed on JEM-2010F, JEOL transmission

electron microscopy. Before the TEM measurement, the H_2-reduced catalysts were cooled to room temperature in H_2 flow and then passivated in 1 vol% O_2/Ar gas mixture for 30 min to prevent bulk oxidation of the Ni nanoparticles. Thermogravimetric (TG) analysis was conducted on a Seiko Instruments EXSTAR TG/DTA 6300. 10 mg sample was used and heated in air (200 mL min^{-1}) from room temperature up to 1000 ^oC (10 ^oC min^{-1}).

2.3. Catalytic measurement

The catalytic measurements are similar to our previous work.[3] Typically, the CO methanation reactions were carried out in a fixed bed reactor at 0.1 MPa. 0.1 g catalyst sample (20−40 mesh) diluted with 5.0 g quartz sands (20−40 mesh) was uploaded in a quartz tube with an inner diameter of 8 mm. The addition of quartz sands was to avoid the generation of hotspot in the catalyst bed. A thermocouple was placed outside of the reactor tube near the middle position of the catalyst bed to measure and monitor the reaction temperature. Prior to the reaction, the catalysts were reduced at 700 ^oC in pure H_2 (100 mL min^{-1}) for 1 h, then cooled to the starting reaction temperature in H_2, and subjected to the mixed H_2 and CO as well as N_2 (as an internal standard) at a molar ratio of $H_2/CO/N_2$=3/1/1. The outlet gas stream from the reactor was cooled using a cold trap. The inlet and outlet gases were analyzed on line by a Micro GC 3000A (Agilent Technologies). The concentrations of H_2, N_2, CH_4 and CO in gas products were detected by a TCD detector connected to a Molecular Sieve column while the concentrations of CO_2, C_2H_4, C_2H_6, C_3H_6 and C_3H_8 were analyzed by another TCD connected to a Plot Q column. A lifetime test of CO methanation was performed at 550 ^oC and 0.1 MPa. The CO conversion, CH_4 selectivity and yield are defined as follows:

$$\text{CO conversion: } X_{CO}(\%) = \frac{F_{CO,in} - F_{CO,out}}{F_{CO,in}} \times 100$$

$$\text{CH}_4\text{ selectivity: } S_{CH_4}(\%) = \frac{F_{CH_4,out}}{F_{CO,in} - F_{CO,out}} \times 100$$

$$\text{CH}_4\text{ yield: } Y_{CH_4}(\%) = \frac{X_{CO} \times S_{CH_4}}{100} = \frac{F_{CH_4,out}}{F_{CO,in}} \times 100$$

Here, X is the conversion of CO, S is the selectivity of CH_4, Y is the yield of CH_4, $F_{i,\,in}$ and $F_{i,\,out}$ are the volume flow rates of species i (i=CO or CH_4) at the inlet and outlet.

In addition, the activation energy was calculated using the Arrhenius equation, as described in our previous works.[3, 17] Typically, the rate and activation energy for CO methanation over the catalyst were measured at 0.1 MPa with a catalyst loading of 0.5 g (20−40 mesh) diluted with 3.0 g quartz sands (20−40 mesh). In order to lower the CO conversion to below 10%, the experiments were performed at different total gas flow rates of 50, 100 and 200 mL min^{-1} in the temperature range of 220−250 ^{o}C. The rate was determined using the following equation:

$$Rate(r) = \frac{F_{CO} \times X_{CO}}{W} = \frac{X_{CO}}{W / F_{CO}}$$

Where F_{CO} represents the flow of the CO in mol s^{-1}, W is the weight of the catalyst in g, and X_{CO} the CO conversion. The variations of X_{CO} with respect to W/F_{CO} were plotted, and then the rates of reaction were calculated at various temperatures from the slope of linear portion.

2.4. Hydrothermal stability measurement

For hydrothermal treatment, the catalysts were loaded into a fixed bed quartz tube reactor under 0.1 MPa. Prior to the treatment, the catalyst (0.5 g) was reduced at 700 ^{o}C in pure H_2 for 1 h and then subjected to 90 vol% H_2O/H_2 (total flow rate of 500 mL min^{-1}) at 600 ^{o}C. After being kept for 8, 12 or 24 h respectively, the catalysts were cooled to room temperature in pure H_2.[18] The obtained

samples were denoted as Cat-yHT (y = 8, 12 and 24), where Cat represents 10NOMA or 10N5ZOMA catalyst, and y represents the different treatment time of the catalysts.

3. Results and discussion

3.1. Characterization of the catalysts

Fig. 1 shows the geometry and morphology features of the reduced Ni–Zr–Al catalysts. It is observed that the typical ordered mesostructure with regular alignment of cylindrical pores along the (100) direction (Fig. 1a, 1c, 1e and 1h) is obtained. In addition, incorporation of nickel and zirconium into OMA via the EISA synthesis does not change the ordered mesoporous structure with *p6mm* hexagonal symmetry. In order to have a closer observation, the TEM images (Fig. 1b, 1d, 1f and 1i) with higher magnifications were recorded. It is seen that the Ni particles in all Ni–Zr–Al catalysts have uniform sizes without any obvious aggregation, and are embedded in the framework with an average size of ca. 4.6 ± 2.5 nm. Addition of proper amounts of zirconia species does not change the Ni particles size obviously. It should be pointed out that it is hardly to distinguish the ZrO_2 species in the reduced Ni–Zr–Al catalysts because of the poor contrast between ZrO_2 and OMA framework or the high dispersion of ZrO_2 species. The HRTEM image of the reduced 10N5ZOMA catalyst is shown in Fig. 1g. The observed lattice spacing of ca. 0.20 nm corresponds to the Ni (111) plane, but there is still no observation of the lattice corresponding to ZrO_2, probably because of its high dispersion in the framework of OMA or poor crystallinity. In addition, the energy-dispersive X-ray spectroscopy (EDS) analyses of the ordered mesostructure domains show clear peaks of Ni, Zr, Al, and O, implying that all the elements have been successfully introduced into the ordered mesoporous materials. The SEM image and the related elemental mapping of the reduced 10N10ZOMA are shown in Fig. 2. The SEM image shows that the sample should be

composed of a single phase, not a mixture according to the morphology and smoothness of the particle surface. The elemental mappings of the reduced 10N10ZOMA confirm that both Ni and Zr species are homogeneously dispersed across the whole catalyst.

<Fig. 1 and 2>

The structure of the calcined sample was further analyzed by N_2 adsorption (Fig. 3). All isotherms are type IV with H1 hysteresis loops, which is the significant feature of ordered mesoporous materials (Fig. 3a).[19] The steep capillary condensation step indicates high uniformity of the formed mesopores. As shown in Fig. 3b, the PSD curves of the Ni–Zr–Al catalysts have only one narrow peak, and the maximum peaks of these curves are all centered at around 12 nm, confirming the high uniformity of the channels in all the catalysts. Table 1 lists the surface area, pore volume and average pore diameter of the calcined samples. All the samples prepared by the EISA method have high specific surface areas, large pore volumes, and an average pore diameter around 10 nm. The surface area becomes larger with addition of more Zr species, because the zirconia precursors used in the preparation of Ni–Zr–Al catalysts can act as swelling agents to increase the micelle size of triblock copolymer.[3, 20]

<Fig. 3>

<Table 1>

Both small-angle XRD (SXRD) and wide-angle XRD (WXRD) patterns of the catalysts are shown in Fig. 4. As seen from SXRD patterns of the calcined catalysts (Fig. 4A), there is a strong peak at around 0.81° corresponding to (100) plane in all the samples, which further confirms the formation of hexagonally ordered mesoporous structure (*p6mm* symmetry),[21] coinciding with the above TEM and N_2 adsorption results. In addition, the WXRD patterns of all the calcined samples have no any apparent diffraction peaks of NiO, ZrO_2 and Al_2O_3, which may be related to their

incorporation into the OMA skeleton, or poor crystallinity, or their high dispersion (Fig. 4B). The WXRD patterns of the reduced catalysts are shown in Fig. 4C. It is seen that the OMA framework is still amorphous even after the high temperature (700 ^{o}C) treatment in a H_2 flow, while three new peaks at around 44.6, 51.8 and 76.6^{o} are observed in these catalysts, corresponding to (111), (200) and (220) planes of metallic Ni (JCPDS 01-070-1849), respectively. The Ni nanoparticle sizes of these catalysts are estimated from the WXRD patterns and listed in Table 1. No matter whether there is the incorporation of Zr species or not, the Ni particles in the ordered mesoporous catalysts are all smaller than 5 nm, indicating their high dispersion in all the catalysts prepared by the EISA method. Moreover, there is still no observation of any diffraction peaks of ZrO_2 even after the 700 ^{o}C H_2-treatment. In order to obtain more evidences about the distribution of the Zr species in the samples, the 40ZA, 40ZOMA and 10N40ZOMA samples were prepared and their wide-angle XRD patterns were measured, and the result is shown in Fig. 5. In the XRD pattern of 40ZA, the diffraction peaks at 30.2, 50.3, 60.3^{o} correspond to tetragonal ZrO_2 (JCPDS 01-080-0965), while the ones at 45.8, 60.5, 67.3^{o} to γ-Al_2O_3 (JCPDS 00-047-1308), but there is no observation of ZrO_2–Al_2O_3 complexes, indicating the ZrO_2 species exists as a separate phase in 40NA. Although the ZrO_2 content is as high as 40 wt%, 40ZOMA exhibits poor crystallinity without any apparent diffraction peaks of ZrO_2 and Al_2O_3 in the XRD pattern. After the NiO loading, only NiO or Ni diffraction peaks are observed in the calcined or reduced 10N40ZOMA sample, indicating without formation of any ZrO_2–NiO complexes. Combining all the above results together, it can be concluded that the ZrO_2 species is distributed in OMA framework as individual particles, not in the form of individual Zr atoms doped in Al_2O_3 or NiO (Al–O–Zr or Ni–O–Zr).

<Fig. 4>

<Fig. 5>

As seen from the reduction profiles of all the samples (Fig. 6a), there is only one reduction peak at around 602 ^{o}C, which can be attributed to the reduction of NiO species in the OMA skeleton with strong interaction with the support.[15] There is no obvious change to the main reduction peaks of the ordered mesoporous Ni–Zr–Al catalyst with increase of ZrO_2 content (except for 10N10ZOMA). The 10N10ZOMA sample has the highest reduction temperature among all the catalysts, probably because the excess ZrO_2 particles cover part of Ni particles which increases the difficulty of their reduction. In addition, as shown in Fig. 6b, the main H_2 desorption peak of all the samples is located at around 182 ^{o}C, which is attributed to the chemisorbed hydrogen on the highly dispersed Ni nanoparticles with high density of surface defects, which often serve as traps for surface hydrogen that are able to reduce the activation energy of hydrogen dissociation.[17, 22] After the ZrO_2 addition, there is an increment in the integrated area of the desorption peak, indicating the presence of more exposed metallic Ni atoms. However, for 10N10ZOMA, the peaks are shifted to lower temperature and the integrated area is decreased again as compared to those of Ni10Cr5-OMA. The reason may be because the sintering degree of Ni particle in this sample is the lowest after the 700^{o}C-reduction due to the stronger metal-support interaction, resulting in the highest surface defect density in Ni particles and the lowest desorption temperature; meanwhile, the partial coverage of surface Ni atoms by excess ZrO_2 can decrease the H_2 adsorption of 10N10ZOMA. Table 1 lists the calculated hydrogen uptakes and the Ni dispersion of the catalysts based on the H_2-TPR and H_2-TPD results. It is seen that the addition of proper amount of ZrO_2 can increase the H_2 uptake and the dispersion of metallic Ni in the Ni–Zr–Al catalysts, and among them, 10N5ZOMA has the highest total H_2 uptake of 83.76 μmol g^{-1} and the Ni dispersion of 12.6%.

<Fig. 6>

3.2. Hydrothermal stability of the catalysts

Considering the fact that water vapor is one of the products of the CO methanantion reaction, and the higher the catalyst efficiency, the higher concentration of steam in product gas will be, a high durability against water vapor is required for the catalyst. Furthermore, steam is often added to the reactant gas mixture to reduce both the hot spots in catalyst bed and the deposited carbon in industry.[1] Therefore, the hydrothermal stability is an important indicator to evaluate a CO methanation catalyst. In this work, the hydrothermal treatment of 10NOMA and 10N5ZOMA was carried out at 600 ^{o}C, 0.1 MPa and weight hourly space velocity (WHSV) of 60000 mL g^{-1} h^{-1} in the presence of 90 vol% H_2O/H_2. After the hydrothermal treatment, all the samples were characterized by N_2 adsorption, and the results are shown in Fig. 7A–B. As shown in Fig. 7A, for 10NOMA, a decrease in the steepness of the capillary condensation step is observed with increasing the time of hydrothermal treatment, indicating the decrease or gradual loss of the mesoporous uniformity during the treatment process. Furthermore, the onsets of hysteresis loops of both 10NOMA-12HT and 10NOMA-24HT are at a relatively high pressure, suggesting the increase of the pore size in these samples. Meanwhile, all the treated 10NOMA samples show a broader pore distribution, especially for 10NOMA-24HT, which confirms the disruption of the ordered mesoporous structure of 10NOMA (Fig. 7B). In contrast, for 10N5ZOMA, there is on obvious change in the adsorption-desorption isotherms as well as the PSD curves even after the 24h-treatment, indicating its excellent hydrothermal stability. Table 2 presents the surface area, pore volume and average pore diameter of the reduced and hydrothermally treated samples. It can be seen that, comparing to the untreated 10N5ZOMA, the hydrothermally treated 10N5ZOMA-24HT retains 69.6% of the specific surface area and 78.6% of the pore volume, and there is almost no increment in the average pore diameter. These changes are much less obvious than those of

10NOMA-24HT. This result confirms the high hydrothermal stability of 10N5ZOMA. In addition, the structure of the hydrothermal treated samples was further analyzed by WXRD (Fig. 7C). For 10NOMA, several new diffraction peaks at 37.6, 45.8 and 67.0^{o} corresponding to λ-Al_2O_3 (JCPDS 00-010-0425) are observed after the hydrothermal treatment, indicating a transition of mesoporous walls from amorphous phase to gamma phase (λ-Al_2O_3). However, for 10N5ZOMA, the OMA framework still remains amorphous phase, indicating that the incorporation of zirconium species can restrain the crystallization of alumina during the hydrothermal treatment at high temperatures. In all, the incorporated Zr species can act effectively as the supporter for the OMA framework and protect OMA from the structural collapse caused by sintering and phase transition during the hydrothermal treatment.[10, 23]

<Fig. 7>

<Table 2>

3.3. Catalytic performances of the catalysts

In order to investigate the effect of Zr addition on the catalytic activity, the CO methanation reaction was carried out in the temperature range of 300−450 ^{o}C at 0.1 MPa using a WHSV of 90000 mL g^{-1} h^{-1}, and the results are shown in Fig. 8a–c. Overall, the catalytic activities of the all the catalysts are similar. After the Zr addition, the CO conversion and CH_4 yield over the 10NxZOMA catalysts are slightly improved; however, the CH_4 selectivity of various catalysts is almost the same at different reaction temperatures, similar to the literature results,[15, 16] which can be explained by the simultaneous promotion of both CO methanation and the side reactions by ZrO_2.[24-26] Among all the catalyst, 10N5ZOMA is the best due to its largest H_2 uptake and Ni dispersion. At the same time, compared to the 10Ni/Al_2O_3 methanation catalyst reported by Gao et al.,[18] 10N5ZOMA is more

active in the total temperature range (except for 400 ^{o}C), although the former was evaluated at a much lower WHSV of 30000 mL g^{-1} h^{-1}, indicating that 10N5ZOMA is a promising catalyst for CO methanation.

<Fig.8>

Meanwhile, the apparent activation energies for CO methanation over the different catalysts were determined and the Arrhenius plots are shown in Fig. 9a. The results show that the activation energies decrease in the order of 10NOMA (69.18 kJ mol^{-1}) > 10N10ZOMA (57.41 kJ mol^{-1}) > 10N2ZOMA (54.37 kJ mol^{-1}) > 10N5ZOMA (42.94 kJ mol^{-1}), which is in good agreement with the activity trend of CO methanation at atmospheric pressure. By comparing with other CO methanation catalysts in the literature,[3, 27] our results are of the same order of magnitude.

<Fig. 9>

The catalyst lifetime is an important indicator to a catalyst, especially the one obtained under the harsh reaction condition. To investigate the catalytic stability of the best catalyst 10N5ZOMA, a 120h-lifetime test was carried out at 550 ^{o}C, 0.1 MPa and high WHSVs of 90000 and 120000 mL g^{-1} h^{-1}, and the results are shown in Fig. 8d. It is seen that both CO conversion and CH_4 selectivity can remain stable at 90000 or 120000 mL g^{-1} h^{-1} through the whole lifetime test, indicating that 10N5ZOMA has a high stability especially at high temperatures and high WHSVs. The spent 10N5ZOMA was further characterized by N_2 absorption, XRD, TEM and TG, and the results are shown in Fig. 7 and 9, respectively. After the lifetime test, the isotherms and the PSD curve of the spent catalyst are still comparable with those of the fresh one (Fig. 7A(i) and Fig. 7B(i)): 10N5ZOMA-spent retains 77.7% of the surface area and 78.6% of the pore volume of the reduced 10N5ZOMA. Moreover, as seen from the TEM image of the spent 10N5ZOMA catalyst, the ordered mesostructure remains almost unchanged and the Ni particles are embedded in the

framework with an average size of ca. 4.2 ± 2.3 nm without any obvious agglomeration (Fig. 9b). Meanwhile, the XRD pattern of the spent catalyst is also similar to that of the reduced one, and the calculated Ni particle size is still smaller than 5 nm (Table 2 and Fig. 7C(i)). These results indicate that the ordered mesoporous structure is hydrothermally stable and well retained after the 120h-lifetime test, which leads to the high resistance toward Ni sintering and coke formation during CO methanation. As reported, the confinement of the highly dispersed Ni particles in the channels and the anchoring of them in the alumina matrix can reduce Ni sintering significantly.[3] The strong metal-support interaction between Ni and the OMA support (Fig. 1 and Fig. 6a) can also suppress the growth of carbon filament which lifts the Ni particle from the support.[17] Indeed, there is no diffraction peak corresponding to graphitic carbon in the XRD pattern (Fig. 7C(i)), no observation of carbon filaments on the surface of the catalysts in the TEM image of the spent catalyst (Fig. 9b), and no crystal lattice corresponding to graphitic carbon in the HRTEM image of the spent 10N5ZOMA (not shown here), indicating that the amount of graphitic carbon is below the detection limit of XRD over the spent 10N5ZOMA catalyst and the deposited carbon is not crystallized Hence, the deposited carbon should be quite small in quantity and most probably in amorphous, similar to that reported in literature.[3] The amount of the deposited carbon on the spent catalysts is determined by TG analysis, and the carbon content in the spent 10N5ZOMA catalyst is estimated to be only 0.2 wt% (Fig. 9c). These results suggest that 10N5ZOMA has excellent anti-coking capacity. Besides the confinement effect, ZrO_2 is able to enhance the dissociation of CO_2 and generate some surface oxygen intermediates, which can further react with the surface carbonaceous species and reduce the carbon deposition on the Ni particles in CO methanation.[14, 16] In short, the superior anti-sintering and anti-coking properties of the Ni–Zr–Al catalyst can be attributed to the confinement effect of the mesopore channels as well as the incorporation of the zirconia promoter.

4. Conclusions

A series of ordered mesoporous Ni–Zr–Al composite oxides with various Zr content have been successfully prepared by the facile one-pot EISA method and are used in CO methanation reaction to produce synthetic natural gas. The obtained materials shows significantly improved hydrothermal stability compared to the ordered mesoporous Ni–Al catalyst, because the incorporation of Zr species acts as the supporter for the OMA framework preventing OMA from the structural collapse caused by sintering and phase transition during the hydrothermal treatment. As demonstrated, this catalyst indeed shows excellent resistance to both Ni sintering and coke formation during the 120h-lifetime test at high temperature. It is believed that both the confinement effect of the mesopore channels and the incorporation of the zirconia promoter contributed to the much improved catalytic property. The work shows that the ordered mesoporous Ni–Zr–Al catalyst is a promising candidate for high temperature reactions such as the CO methanation.

Acknowledgments

The authors gratefully acknowledge the supports from the National Natural Science Foundation of China (no. 21476238), the National Basic Research Program (2014CB744306), the National High Technology Research and Development Program 863 (no. SS2015AA050502), and "Strategic Priority Research Program" of the Chinese Academy of Sciences (nos. XDA07010100 and XDA07010200).

References

1. J. Kopyscinski, T. J. Schildhauer and S. M. A. Biollaz, *Fuel*, 2010, **89**, 1763-1783.

2. J. J. Gao, Q. Liu, F. N. Gu, B. Liu, Z. Y. Zhong and F. B. Su, *RSC Adv.*, 2015, **5**, 22759-22776.

3. Q. Liu, J. J. Gao, F. N. Gu, X. P. Lu, Y. J. Liu, H. F. Li, Z. Y. Zhong, B. Liu, G. W. Xu and F. B. Su, *J. Catal.*, 2015, **326**, 127-138.

4. C. H. Bartholomew, *Catal. Rev.*, 1982, **24**, 67-112.

5. C. H. Bartholomew, *Appl. Catal. A*, 2001, **212**, 17-60.

6. A. M. Cao, R. W. Lu and G. Veser, *Phys. Chem. Chem. Phys.*, 2010, **12**, 13499-13510.

7. S. R. Li and J. L. Gong, *Chem. Soc. Rev.*, 2014, **43**, 7245-7256.

8. Q. Yuan, A. X. Yin, C. Luo, L. D. Sun, Y. W. Zhang, W. T. Duan, H. C. Liu and C. H. Yan, *J. Am. Chem. Soc.*, 2008, **130**, 3465-3472.

9. S. M. Morris, P. F. Fulvio and M. Jaroniec, *J. Am. Chem. Soc.*, 2008, **130**, 15210-15216.

10. X. Y. Wang, D. H. Pan, M. Guo, M. He, P. Y. Niu and R. F. Li, *Mater. Lett.*, 2013, **97**, 27-30.

11. F. H. Meng, Z. Li, F. K. Ji and M. H. Li, *Int. J. Hydrogen Energy,* 2015, **40**, 8833-8843.

12. W. Y. Teoh, D. E. Doronkin, G. K. Beh, J. A. H. Dreyer and J. D. Grunwaldt, *J. Catal.*, 2015, **326**, 182-193.

13. J. Z. Yang, J. Ren, H. L. Guo, X. Qin, B. Y. Han, J. Y. Lin and Z. Li, *RSC Adv.*, 2015, **5**, 59935-59945.

14. H. L. Lu, X. Z. Yang, G. J. Gao, K. B. Wang, Q. Q. Shi, J. Wang, C. H. Han, J. Liu, M. Tong, X. Y. Liang and C. F. Li, *Int. J. Hydrogen Energy,* 2014, **39**, 18894-18907.

15. Q. Liu, J. J. Gao, M. J. Zhang, H. F. Li, F. N. Gu, G. W. Xu, Z. Y. Zhong and F. B. Su, *RSC Adv.*, 2014, **4**, 16094-16103.

16. Q. Liu, F. N. Gu, J. J. Gao, H. F. Li, G. W. Xu and F. B. Su, *J. Energy Chem.*, 2014, **23**, 761-770.

17. Q. Liu, F. N. Gu, X. P. Lu, Y. J. Liu, H. F. Li, Z. Y. Zhong, G. W. Xu and F. B. Su, *Appl. Catal. A*, 2014, **488**, 37-47.

18. J. J. Gao, C. M. Jia, J. Li, M. J. Zhang, F. N. Gu, G. W. Xu, Z. Y. Zhong and F. B. Su, *J. Energy Chem.*, 2013, **22**, 919-927.

19. L. L. Xu, Z. L. Wang, H. L. Song and L. J. Chou, *Catal. Commun.*, 2013, **35**, 76-81.

20. S. M. Grant and M. Jaroniec, *J. Mater. Chem.*, 2012, **22**, 86-92.

21. Q. Yuan, L. L. Li, S. L. Lu, H. H. Duan, Z. X. Li, Y. X. Zhu and C. H. Yan, *J. Phys. Chem. C,* 2009, **113**, 4117-4124.

22. J. Liu, C. M. Li, F. Wang, S. He, H. Chen, Y. F. Zhao, M. Wei, D. G. Evans and X. Duan, *Catal. Sci. Technol.*, 2013, **3**, 2627-2633.

23. Q. P. Sun, Y. Zheng, Z. H. Li, Y. Zheng, Y. H. Xiao, G. H. Cai and K. M. Wei, *Phys. Chem. Chem. Phys.*, 2013, **15**, 5670-5676.

24. G. A. Somorjai and M. Yang, *Top. Catal.*, 2003, **24**, 61-72.

25. G. A. Somorjai and Y. G. Borodko, *Catal. Lett.*, 2001, **76**, 1-5.

26. J. J. Gao, Y. L. Wang, Y. Ping, D. C. Hu, G. W. Xu, F. N. Gu and F. B. Su, *RSC Adv.*, 2012, **2**, 2358-2368.

27. X. P. Lu, F. N. Gu, Q. Liu, J. J. Gao, Y. J. Liu, H. F. Li, L. H. Jia, G. W. Xu, Z. Y. Zhong and F. B. Su, *Fuel Process. Technol.*, 2015, **135**, 34-46.

Figure & Table Captions

Fig. 1 TEM images and the corresponding EDS spectra of the reduced samples: (a and b) 10NOMA, (c and d) 10N2ZOMA, (e–g) 10N5ZOMA, and (h and i) 10N10ZOMA.

Fig. 2 SEM image of the reduced 10N10ZOMA (a) and elemental mapping images of Al (b), Zr (c), and Ni (d).

Fig. 3 N_2 adsorption isotherms (a) and PSD curves (b) of the calcined catalysts (For clarity, the isotherms of 10NOMA, 10N2ZOMA, 10N5ZOMA, and 10N10ZOMA were vertically shifted for 800, 500, 280, and 0 $cm^3\ g^{-1}$, respectively.).

Fig. 4 Small-angle XRD (A) and wide-angle XRD (B) patterns of the calcined samples and wide-angle XRD patterns of the reduced samples (C): (a) 10NOMA, (b) 10N2ZOMA, (c) 10N5ZOMA, and (d) 10N10ZOMA.

Fig. 5 Wide-angle XRD patterns of the calcined 40NA, 40ZOMA and 10N40ZOMA as well as the reduced 10N40ZOMA.

Fig. 6 H_2-TPR profiles (a) and H_2-TPD profiles (b) of the catalysts.

Fig. 7 N_2 adsorption isotherms (A), PSD curves (B) and wide-angle XRD patterns (C) of the reduced and hydrothermally treated catalysts: (a) reduced 10NOMA, (b) 10NOMA-8HT, (c) 10NOMA-12HT, (d) 10NOMA-24HT, (e) reduced 10N5ZOMA, (f) 10N5ZOMA-8HT, (g) 10N5ZOMA-12HT, (h) 10N5ZOMA-24HT and (i) 10N5ZOMA-spent (For clarity, the isotherms of reduced 10NOMA, 10NOMA-8HT, 10NOMA-12HT, 10NOMA-24HT, reduced 10N5ZOMA, 10N5ZOMA-8HT, 10N5ZOMA-12HT, 10N5ZOMA-24HT and 10N5ZOMA-spent were vertically shifted for 1530, 1355, 1110, 925, 785, 615, 445, 290 and 0 $cm^3\ g^{-1}$, respectively.).

Fig. 8 Catalytic properties of the catalysts at 90000 mL $g^{-1}\ h^{-1}$, 0.1 MPa: (a) CO conversion, (b) CH_4 selectivity, and (c) CH_4 yield; and lifetime test of 10N5ZOMA at 550 ^oC, 0.1 MPa (d). (Note:

the reference catalyst 10Ni/Al_2O_3 was evaluated at 30000 mL g^{-1} h^{-1}, 0.1 MPa).

Fig. 9 Arrhenius plots for CO methanation on different Ni catalysts (a), TEM image of the spent 10N5ZOMA catalyst (b), and TG curves of the reduced and spent catalysts in air (c).

Table 1 Physical and chemical properties of the samples

Table 2 Physical and chemical properties of the samples

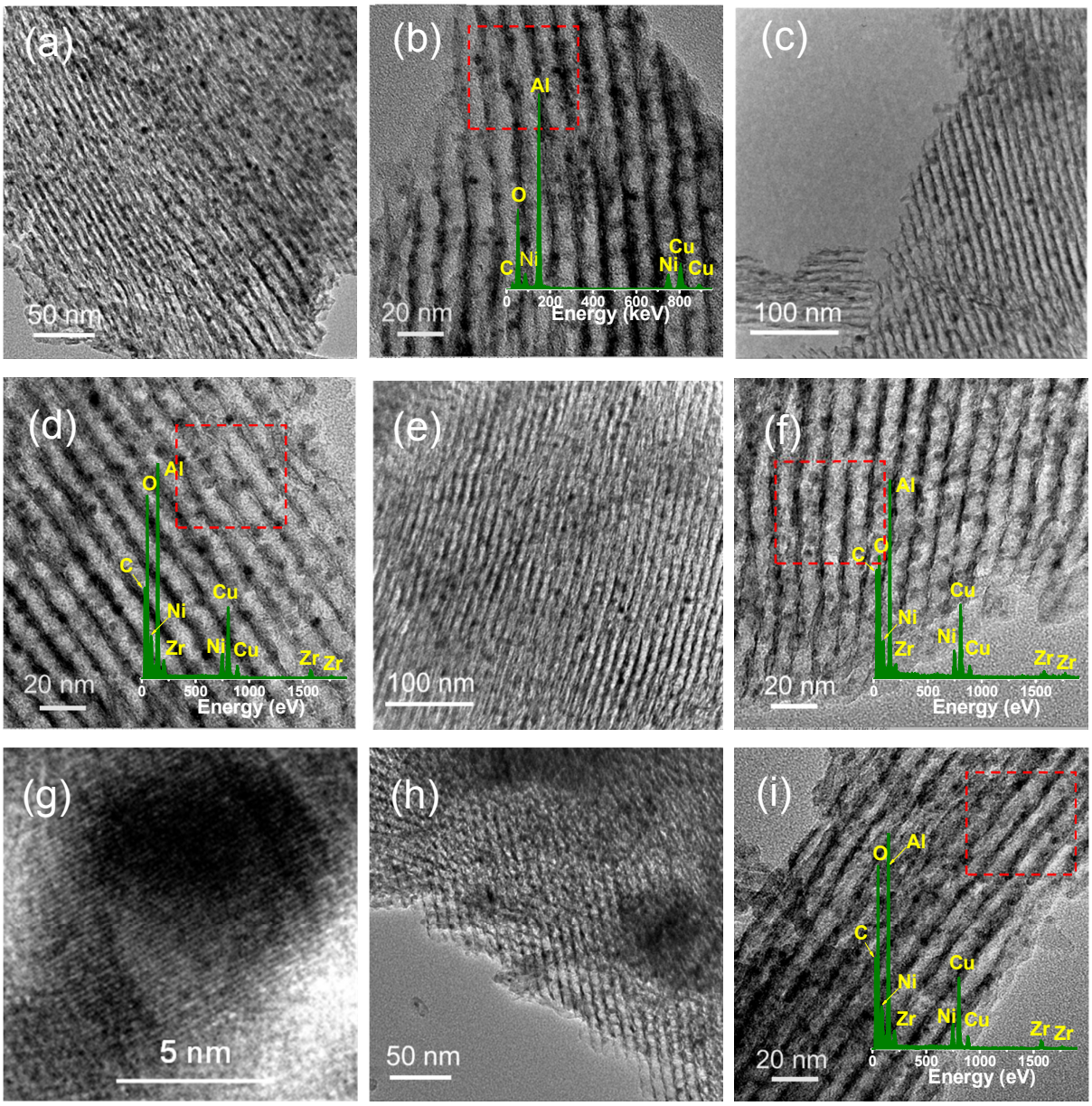

Fig. 1

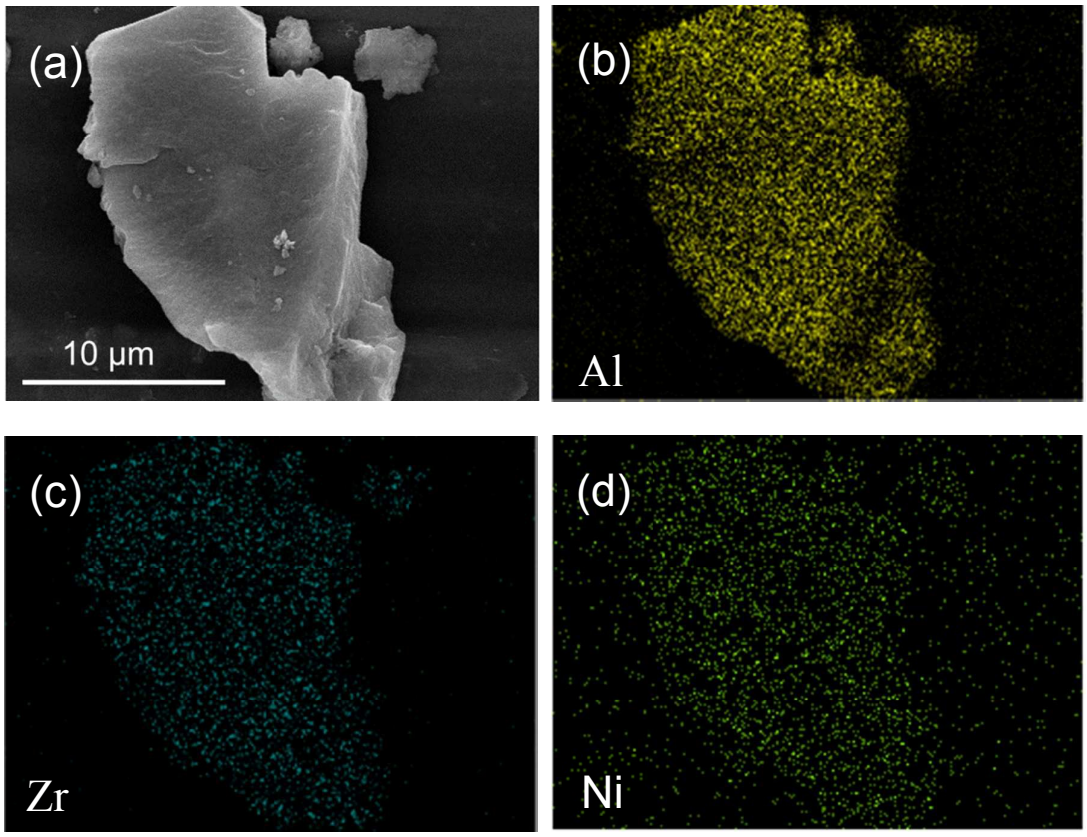

Fig. 2

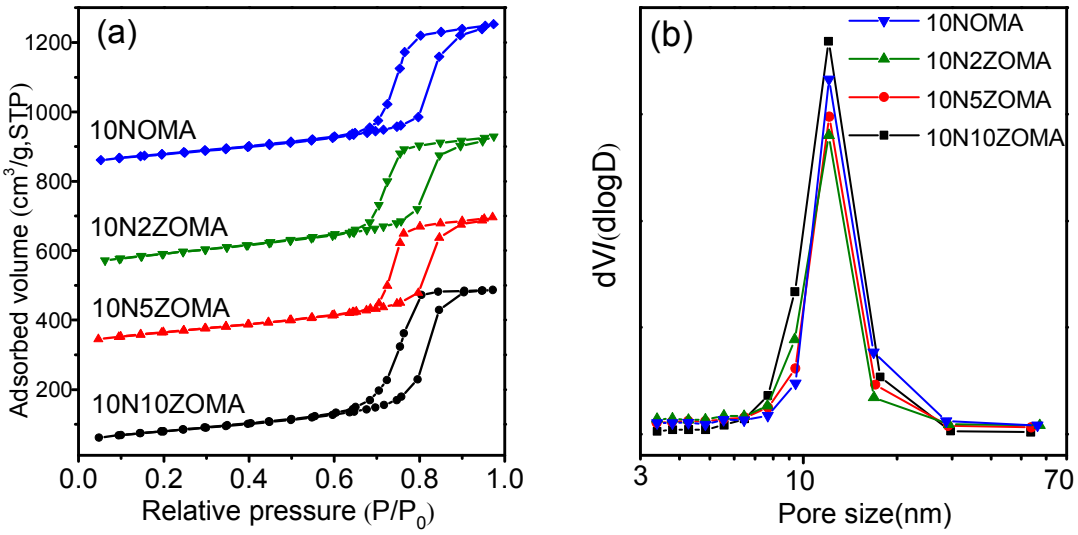

Fig. 3

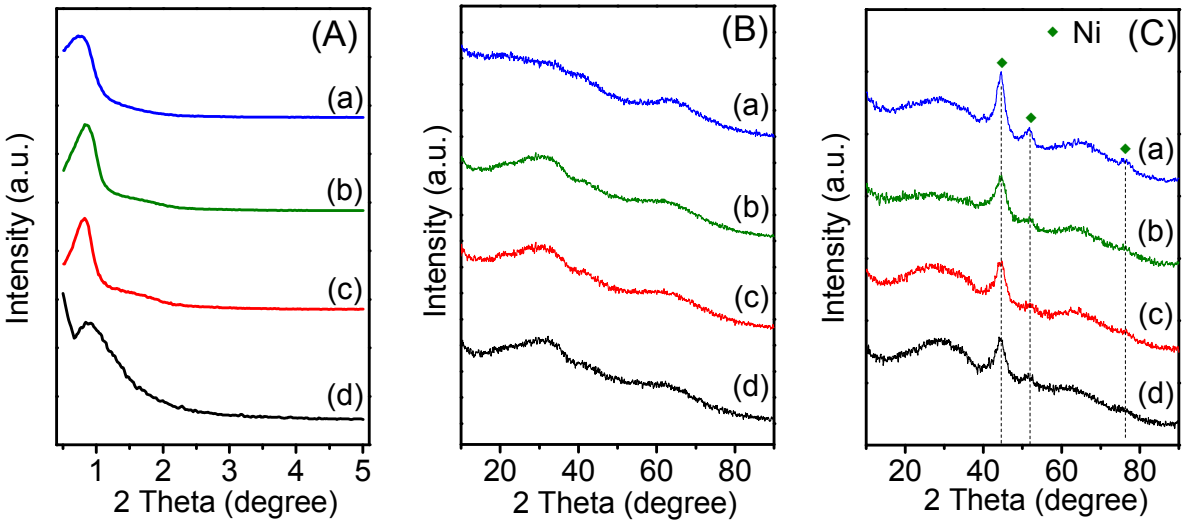

Fig. 4

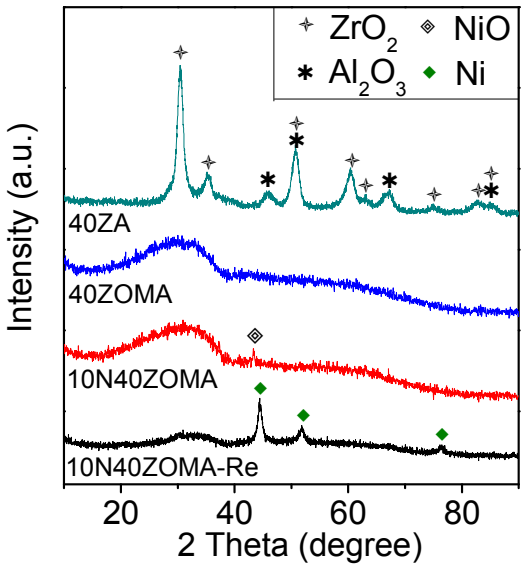

Fig. 5

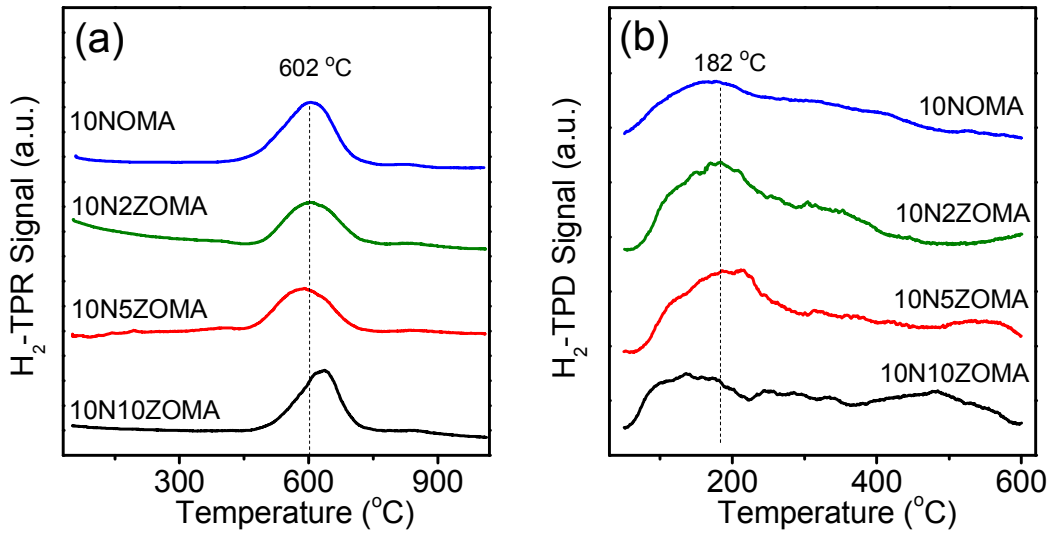

Fig. 6

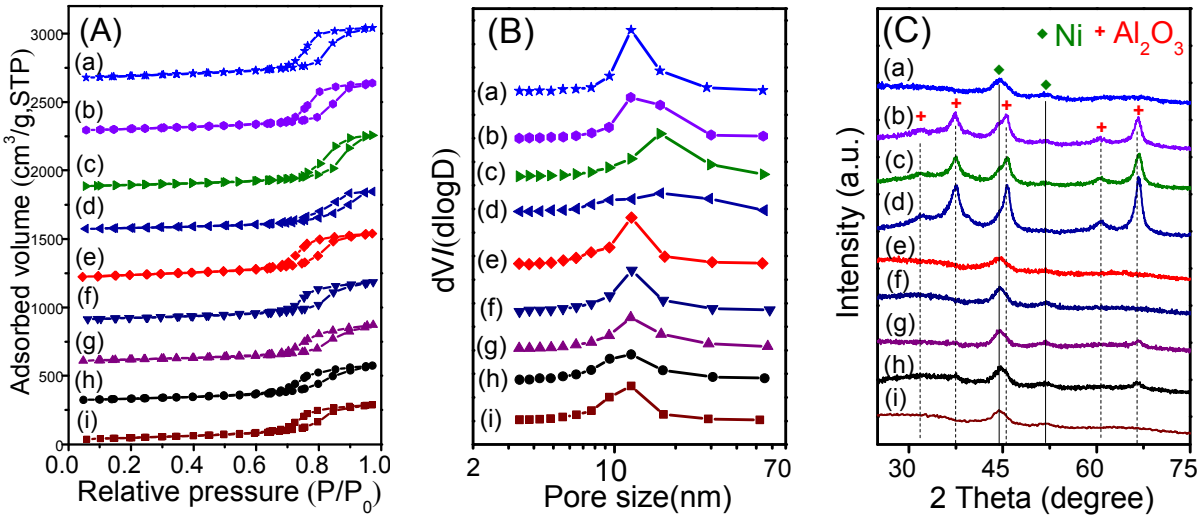

Fig. 7

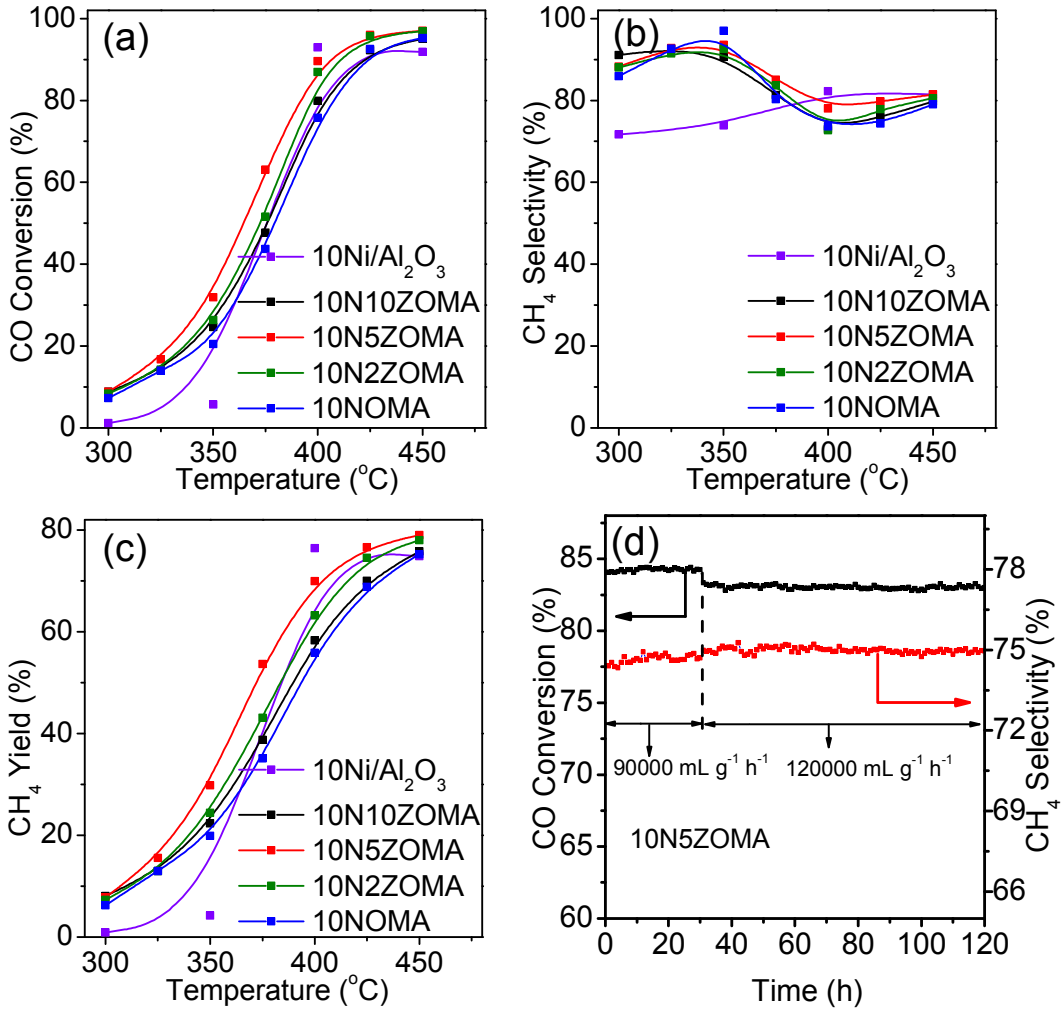

Fig. 8

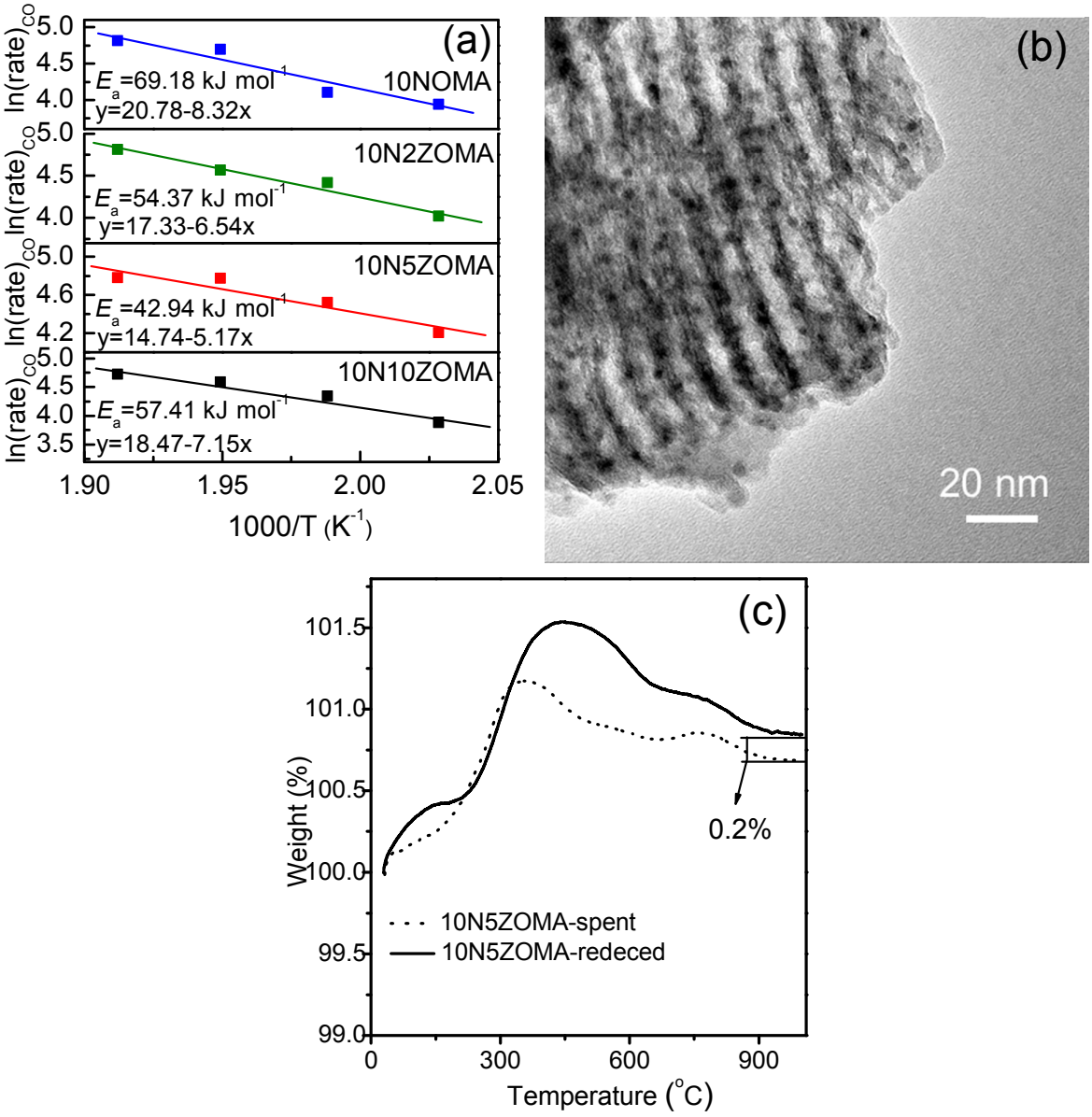

Fig. 9

Table 1

Sample	S_{BET}[a] ($m^2\ g^{-1}$)	V_P[b] ($cm^3\ g^{-1}$)	D_P (nm)[c]	Ni particle size (nm)[d]	H_2 uptake ($\mu mol\ g^{-1}$)	D (%)[e]
10NOMA	271.1	0.70	10.3	< 5	58.4	8.8
10N2ZOMA	321.8	0.66	8.2	< 5	69.8	10.5
10N5ZOMA	299.5	0.64	8.6	< 5	83.7	12.6
10N10ZOMA	277.5	0.75	10.8	< 5	65.5	9.9

[a] S_{BET}, surface area of the calcined sample derived from BET equation.

[b] V_P, pore volume of the calcined sample obtained from the volume of nitrogen adsorbed at the relative pressure of 0.97.

[c] D_P, average pore diameter of the calcined sample derived from BJH method using the following equation $D_P = 4 \times \frac{V_P}{S_{BET}}$.

[d] Estimated from the XRD diffraction peak (2θ = 44.6) using the Debye-Scherrer equation. Considering the limitation of this calculation method, the Ni particle size was denoted as '< 5.0' when the calculated value was smaller than 5.0 nm.

[e] Ni dispersion calculated based on the H_2-TPR and H_2-TPD results.

Table 2

Sample	S_{BET}[a] ($m^2\ g^{-1}$)	V_P[b] ($cm^3\ g^{-1}$)	D_P (nm)[c]	Ni particle size (nm)[d]
10NOMA[e]	209.9	0.63	12.1	< 5
10NOMA-8HT	170.6	0.59	13.9	5.8
10NOMA-12HT	150.8	0.63	16.7	7.8
10NOMA-24HT	124.8	0.46	14.9	9.2
10N5ZOMA[e]	218.1	0.56	11.3	< 5
10N5ZOMA-8HT	165.7	0.48	11.6	< 5
10N5ZOMA-12HT	155.0	0.46	11.8	< 5
10N5ZOMA-24HT	151.8	0.44	11.6	< 5
10N5ZOMA-spent[f]	169.4	0.44	11.5	< 5

[a] S_{BET}, surface area of the calcined sample derived from BET equation.

[b] V_P, pore volume of the calcined sample obtained from the volume of nitrogen adsorbed at the relative pressure of 0.97.

[c] D_P, average pore diameter of the calcined sample derived from BJH method using the following equation $D_P = 4 \times \frac{V_P}{S_{BET}}$.

[d] Estimated from the XRD diffraction peak (2θ = 44.6) using the Debye-Scherrer equation. Considering the limitation of this calculation method, the Ni particle size was denoted as '< 5.0' when the calculated value was smaller than 5.0 nm.

[e] Reduced catalysts at 700 °C in H_2 flow for 1 h.

[f] Catalysts recovered after 120h-lifetime test.

Graphical Abstract

The ordered mesoporous Ni–Zr–Al catalyst exhibits high hydrothermal stability as well as high anti-coking and anti-sintering properties, due to the confinement effect of the mesopore channels and the incorporation of the ZrO_2 species.